

36 Gb/s Narrowband Photoreceiver for mmWave Analog Radio-over-Fiber

Laurens Bogaert, Haolin Li, Kasper Van Gasse, Joris Van Kerrebrouck,
Johan Bauwelinck, Gunther Roelkens, and Guy Torfs

Abstract—Migrating toward higher frequencies and densification of the communication cells are two key enablers for increased wireless data rates. To make these trends economically viable, centralized architectures based on radio-over-fiber (RoF) are explored. This paper describes the design of a photoreceiver that can be applied at the remote radio head in a 28 GHz analog RoF link. The devised photoreceiver comprises a Ge-on-Si photodetector and co-designed GaAs low noise amplifier offering 24 dB gain, corresponding to 224 V/W external conversion gain, over a 3-dB bandwidth between 23.5 and 31.5 GHz. The associated noise figure is 2.1 dB and an output referred third order intercept point up to 26.5 dBm can be obtained with a power consumption of 303 mW. Two possible applications are demonstrated in this paper. First, the photoreceiver is tested in a 5G New Radio environment resulting in rms-EVM values below 2.46/3.47% for 100/400-MBaud 16-QAM transmission over the 24.25–29.5 GHz band. Secondly, very high data rates can also be supported, demonstrated by a 36 Gb/s link with an rms-EVM of 5.2%.

Index Terms—Hybrid Integration, Low Noise Amplifier, Optoelectronic, Radio-over-Fiber, Resonant Photoreceiver

I. INTRODUCTION

NEXT generation wireless mobile networks will require the deployment of increasingly faster communication links. Achieving the required enhanced data rates can be met by migrating toward (near-)mmWave frequencies as well as having a densification of the communication cells [1]. Direct densification of the network results in increased cost of the network and is thus to be avoided. To make the miniaturization of the wireless cell sizes viable, centralized approaches are key. Radio-over-Fiber (RoF) has been proposed as a possible transmission scheme to push most of the complexity to a centralized base station (BS) [2]. Nowadays, RoF is typically implemented digitally with the Common Public Radio Interface (CPRI) [3]. Evolving toward Analog RoF (ARoF) enables low-complexity, low-cost remote radio heads (RRHs)

This work was supported by the Ghent University Special Research Fund (BOF14/GOA/034), the Methusalem funding of the Flemish government, the Air Force Office of Scientific Research (AFOSR) (FA95501810015), the European Research Council Grant ATTO (695495), and by the H2020 5GPPP Phase II project 5G-PHOS (761989).

L. Bogaert, H. Li, J. Van Kerrebrouck, J. Bauwelinck and G. Torfs are with the Department of Information Technology (INTEC), IDLab, Ghent University-imec, Ghent, 9052 Belgium (e-mail: laurens.bogaert@ugent.be; haolin.li@ugent.be; joris.vankerrebrouck@ugent.be; johan.bauwelinck@ugent.be; guy.torfs@ugent.be).

L. Bogaert, K. Van Gasse, G. Roelkens are with the Department of Information Technology (INTEC), Photonics Research Group, Ghent University-imec, Ghent, 9052 Belgium (e-mail: laurens.bogaert@ugent.be; kasper.vangasse@ugent.be; gunther.roelkens@ugent.be).

Manuscript received January XX, XXXX; revised January XX, XXXX.

that are required to make such a small cell communication network feasible. Furthermore, ARoF offers improved spectral efficiency.

The downlink of an ARoF link starts from the BS, where the RF signal is generated and modulated on an optical carrier. This optical signal is subsequently transported over standard single mode fiber (SSMF) to the targeted RRH. When the signal arrives at the RRH it is converted back to the electrical domain, amplified to the desired signal strength and passed on to the antenna to bridge the wireless link.

This work covers the design of such a photoreceiver, i.e. the combination of the opto-electronic conversion and RF amplification. A hybrid system has been constructed where wire bonding is used to interconnect the photodetector and amplifier. The former is fabricated on the iSiPP50G silicon photonics platform [4] which enables low-cost manufacturing of such a device in high volume while allowing integration of other optical functionality on the same circuit [5]. The RF amplifier is implemented using a 0.1 μm pHEMT GaAs technology. Providing sufficiently high output power levels to the antenna requires the usage of III-V materials for the design of the amplifier. There exist several platforms (GaAs, InP, GaN, ...) offering distinct advantages and disadvantages. In this work, GaAs was chosen since it offers high-frequency, moderately high-power amplification at a much lower cost than other III-V compounds. Additionally, the GaAs industry is mature, offers a high yield and reproducibility [7]. An added benefit is the availability of high-quality passives because of the high substrate resistivity.

This paper is an extension of our work presented at *ECOC 2019* [8]. In Section II, a qualitative comparison will be provided between broadband and resonant amplifiers for narrowband communication. Section III will describe the design of the low noise amplifier (LNA). Subsequently the LNA performance is presented in section IV and compared to the state of the art in section V. In section VI, the photoreceiver is used in link experiments for two applications. Firstly, the performance for 5G New Radio is covered. Secondly, the potential use of the photoreceiver in high data rate applications is verified. Finally, conclusions are drawn in Section VII.

II. RESONANT VERSUS BROADBAND PHOTORECEIVER

Typical implementations of optical receivers in radio over fiber links make use of a broadband transimpedance amplifier (TIA). The main topology used for designing a TIA is adding a feedback resistor between input and output of an open loop

amplifier [9]. In this way, high bandwidth can be combined with low noise behavior. At the input of the TIA a virtual ground is created. Consequently, the current generated in the photodetector will almost completely enter the TIA and will be amplified and converted to a voltage with amplification factor Z_T , the transimpedance gain. Such a TIA is usually designed to offer gain from DC to high frequencies with maximal gain flatness. Using a TIA for narrowband communication requires the TIA to have a bandwidth exceeding the carrier frequency of the narrowband signal while gain is only required in the part of the spectrum where the RF signal is present [10]. Low pass amplification is important for digital communication in e.g. data centers, however, it is typically suboptimal for the narrowband schemes used in wireless communication because of unnecessary constraints imposed by the transimpedance limit [11]. In [12], resonant inductive peaking at the input of a TIA is added to boost the performance of conventional broadband transimpedance amplifiers for narrowband communication.

A different approach to provide amplification to the output of a photodetector comprises a dedicated LNA to provide optimal power transfer from the RF signal generated in the photodetector to the desired load impedance in the frequency range of interest. This is in contrast to the broadband amplification stage that provides suboptimal current-to-voltage conversion from DC up to the maximum frequency of interest [13]. This difference becomes even more important when higher RF carriers are envisioned. Increasing the requirement on bandwidth of the TIA will namely require a lower resistance in the feedback path and hence result in lower gain and larger thermal noise contribution [9]. The narrowband LNA design methodology will allow for a more optimal trade-off between the minimization of noise and maximization of gain, especially at higher frequencies. An added benefit is the fact that parasitics can be resonated out (e.g. wirebond inductance) in a narrowband design while they deteriorate the performance in broadband amplifiers, making the LNA more high-frequency friendly than traditional TIA configurations. The main difficulty of the LNA design is the significant sensitivity on the exact values of the parasitics, i.e. a shifted passband is detrimental due to the resonant nature of the circuit. A second issue is the need for a dedicated design depending on the targeted frequency band and adopted photodetector.

III. PHOTORECEIVER DESIGN & ASSEMBLY

The presented narrowband photoreceiver comprises a Ge photodetector and a GaAs LNA as can be seen in Fig. 1. In this section, the design of a three stage LNA is discussed based on a readily available Ge-on-Si waveguide-integrated vertical pin photodetector from imec's iSiPP50G silicon photonics platform [4]. The LNA has been designed in a $0.1\ \mu\text{m}$ pHEMT GaAs technology [6]. As a first step in the design process of the photoreceiver, a model of the input circuit needs to be derived. This equivalent model for the input circuit consists of two parts: the photodetector and the wirebonds interconnecting the photonic and electronic IC. The combined effect is depicted in Fig. 2. The photodetector can be approximated by a parallel combination of a current

source I_{PD} and a junction capacitance C_j . Losses in the photodetector are modelled by adding a series resistance R_s to this parallel combination. This resistance is approximately independent of the photodetector voltage while the junction capacitance decreases with increasing reverse voltage. The photocurrent I_{PD} is proportional to the incident optical power with proportionality factor \mathcal{R} . The responsivity \mathcal{R} is 0.8 A/W at 1550 nm for the adopted photodetector and coupling to the chip is done by using a grating coupler which results in about 5 dB insertion loss. Furthermore it should be noted that all the results given in this paper are for TE polarized light due to the polarization sensitive nature of the grating couplers.

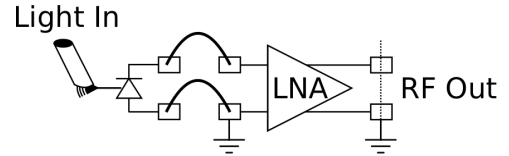


Fig. 1: Schematic overview of the photoreceiver.

For the adopted photodetector, the series resistance is $45\ \Omega$ and the junction capacitance changes between 71 and 47 fF for photodetector reverse voltage of 0 and 3 V respectively. The LNA was designed for a nominal reverse voltage of 1 V resulting in a 55 fF junction capacitance. A second part of the model is the wirebond inductance L_{wb} . This inductance is modelled by approximating the wirebond pair as a current loop consisting of two conductors of $25\ \mu\text{m}$ diameter spaced $100\ \mu\text{m}$ apart and having a length of around $600\ \mu\text{m}$. Assuming these dimensions, an inductance value of 495 pH is found [14]. Adopting these values results in a nominal source impedance Z_s of $45-j12.9\ \Omega$ at 28.5 GHz. To compensate for changes in the wirebond length, the reverse voltage of the photodetector can be adjusted to change the junction capacitance accordingly.

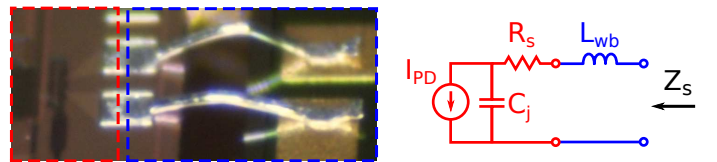


Fig. 2: Input circuit seen by the LNA consisting of a photodetector-wirebond combination.

In the following subsections, the different stages of the LNA will be discussed briefly. A three stage amplifier is optimized for operation in the 27.5–29.5 GHz band. The source impedance Z_s is $45-j12.9\ \Omega$ at 28.5 GHz, and it is required to have an internal bias tee at the input of the LNA to enable biasing of the photodetector. The targeted load impedance is $50\ \Omega$ and should be DC blocked. During the design, the high frequency behavior of parasitics and passives were estimated using the 2.5D solver ADS momentum.

During the design of the photoreceiver, 5G wireless communication in the 28 GHz band was typically limited to 27.5 – 29.5 GHz and therefore it was mainly designed for optimal performance in the aforementioned spectral range. However, the band has recently been extended to 24.25 – 29.5 GHz, and

therefore this paper will also explore the performance of the receiver in the extended 28 GHz band.

A. First Stage

For the first stage, the trade-off between noise and gain matching is of paramount importance. Good noise matching is required to get a low noise behavior while high gain is required to minimize influence of noise induced by subsequent stages and to get good overall gain. While gain and noise characteristics are critical, stability should be preserved and good matching at in- and output is required to avoid ringing. To get good noise and gain matching while trading in excess output return loss for improved input return loss, the design strategy discussed in [15] was adopted. The final result of the first stage is depicted in Fig. 3, where the length of the transmission line segments are given in degrees at 28.5 GHz. Source degeneration is used to bring the optimal source impedances for noise and gain matching closer together and consequently get a better overall gain-noise performance. To ensure stability at the operation frequency, a shunt resistor is added at the drain. Subsequently, a parallel RLC network is added to extend this up to the transition frequency f_T of the transistor. The pHEMT uses a zero volt DC gate-source level to allow self-biasing of the gate. This technique reduces the complexity of the amplifier and is also adopted in the subsequent stages. The input matching network of the first stage contains a bias tee to enable biasing of the photodetector and to make sure that any DC current generated by the photodetector is not saturating the amplifier. An important component in the design of the discussed LNA is the RF Ground (RFG) which is an over-via-capacitor, i.e. a parallel plate capacitor on top of a via. By correctly dimensioning the capacitor it resonates with the via inductance such that the RFG acts as a ground at the operation frequency and as an open at DC. The global ground indicated by GND in Fig. 3 will on the contrary act as a ground at all frequencies.

B. Second Stage

The design of the second stage was done in a similar fashion as the first stage. The main difference concerns the fact that the source impedance follows from the output impedance of the first stage in combination with the interstage matching network. The final implementation of this second stage is shown in Fig. 4.

C. Third Stage

For the final stage, an identical design strategy as with the 2nd stage was followed. Unconditional stability is ensured by adding a $7.5\ \Omega$ resistor in series with the gate and the resulting schematic of the final stage is depicted in Fig. 5. A $50\ \Omega$ transmission line is present at the output of the LNA to ensure compatibility with predefined MPW chip sizes. This transmission line segment, indicated by TL_{MPW} , is therefore not a functional part of the LNA.

D. Final Implementation

The final design of the LNA is shown in Fig. 6 and consists of 3 amplification stages that can be biased independently. In practice, however, these DC lines will be connected to a single power supply V_D to minimize biasing complexity. The input of the amplifier is wirebonded to a Ge-on-Si photodetector and is connected to V_{PD} with an internal bias tee to counter inductance variations and source DC current generated by the photodetector. At the output, AC coupling is present and a $50\ \Omega$ load is expected. The photoreceiver assembly is shown in Fig. 7 where the DC pads of the LNA are connected to PCB traces with chip capacitors of 10 and 100 nF for additional decoupling.

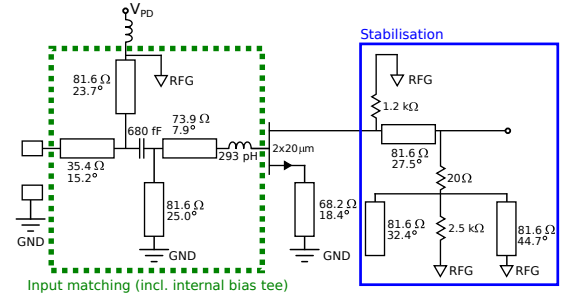


Fig. 3: Amplifier stage 1 (RFG: RF ground).

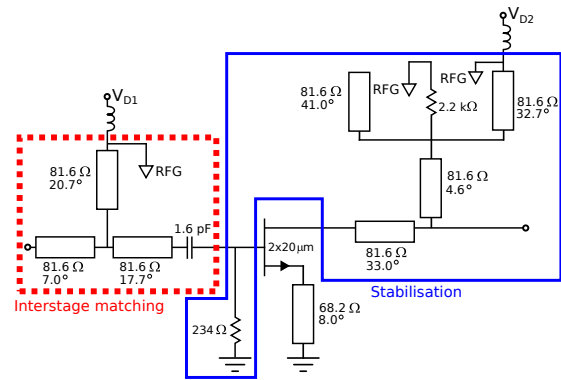


Fig. 4: Amplifier stage 2.

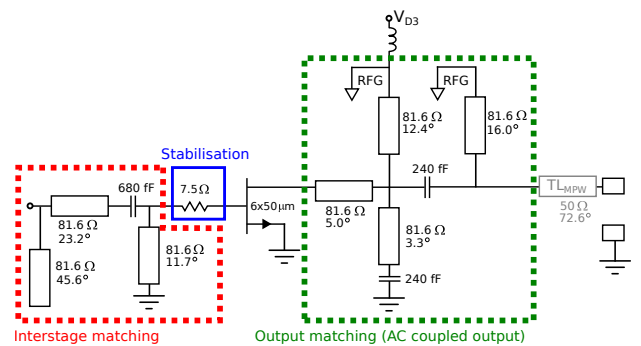


Fig. 5: Amplifier stage 3.

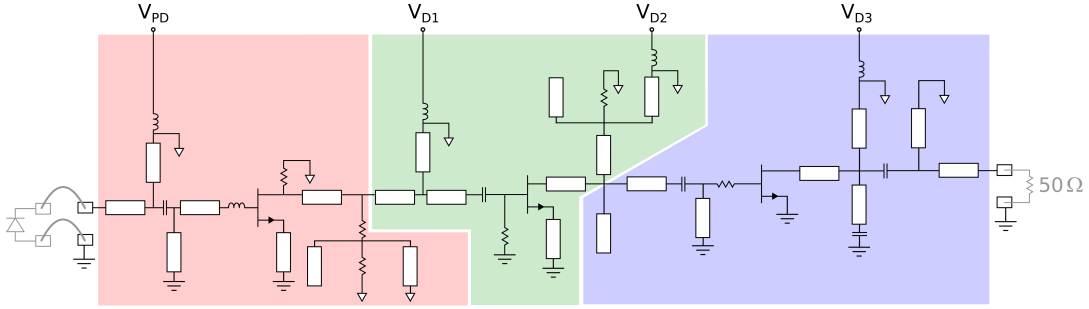


Fig. 6: Overall schematic of the 3-stage near-mmWave low noise amplifier.

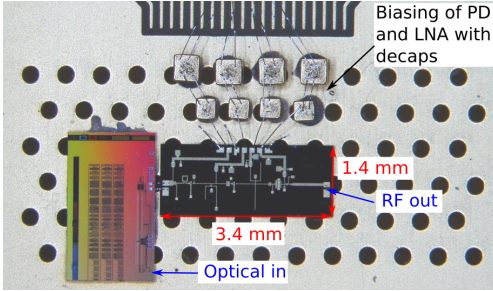


Fig. 7: Narrowband photoreceiver assembly.

IV. LNA PERFORMANCE

A. Small Signal Behavior

To determine the S-parameters of the LNA, a setup with a vector network analyzer (VNA) and 2 probes was used after which the influence of the probes was compensated for using a SOLT calibration substrate. This provides the scattering parameters of the device under test (DUT) in a $50\ \Omega$ environment. As the source is not $50\ \Omega$, these S-parameters give a distorted interpretation. To give a result that is easier to interpret, S-parameter transformations are performed [16] to display the S-parameters for the actual source impedance (Fig. 2). The adopted output reference impedance remains $50\ \Omega$ as this is also the load for which the LNA was designed. The results are compared with simulations in Fig. 8 (a)-(c) after the aforementioned source reference transformation to the photodiode-wirebond combination. Both the simulated and measured small signal behavior in Fig. 8 (a)-(c) are given for a 2 V supply. Simulations and measurements agree very well apart from the presence of an additional dip in the measured S_{11} of the LNA. In Fig. 9, the measured and simulated S_{11} are shown together with the conjugate match of the measured source impedance (Fig. 2) for a $50\ \Omega$ reference. The measured and simulated curves follow a similar shape but deviate slightly, resulting in the extra dip in S-parameters. This is potentially caused by some small deviations in the input matching network.

Figure 8(a) shows that the measured S_{21} ranges between 24.0 to 23.7 dB in the 27.5 to 29.5 GHz range, which corresponds with 884 to 788 V/A transimpedance gain from the current source I_{PD} to a $50\ \Omega$ load. Taking into account the responsibility of the adopted photodetector (0.8 A/W at 1550 nm), a

conversion gain of 707 to 630 V/W is obtained from the input of the photodetector to a $50\ \Omega$ load. The external conversion gain from fiber to the output of the LNA is 224 to 199 V/W due to the 5 dB coupling loss caused by the grating coupler. This can be enhanced by making use of edge coupling to reduce the coupling loss to about 1.2 dB which would result in a conversion gain of 536 to 478 V/W. The measured 3-dB cut-off frequencies are situated at 24.4 and 31.2 GHz. Input and output return loss stay below -14.3 and -14.4 dB respectively in the 27.5 – 29.5 GHz range and the -10 dB return loss bandwidth covers 24.3 to 30.5 GHz at the input and 26.2 to 31.6 GHz at the output. In Fig. 8(d), the transfer characteristic of the entire photoreceiver is presented [8]. A similarly shaped transfer function is obtained but with slightly shifted 3-dB frequencies (23.5 and 31.5 GHz). This slight change in 3 dB bandwidth can be attributed to the fact that the photoreceiver measurement includes the behavior of the actual wirebonds while the S-parameters shown in Fig. 8 (a)-(c) approximate the wirebond pair as a single inductor. Additionally, it can be seen in Fig. 8(d) that the change from a 2 V (*low power consumption setting*) to a 3 V supply (*high linearity setting*) has a negligible impact on the transfer function of the photoreceiver.

B. Linearity

Initial simulations showed an expected output referred third order intercept point (OIP3) of 20.4 and 24.1 dBm at 28.5 GHz for respectively 2 and 3 V supplied to the drain of the three stages. The corresponding output referred 1-dB compression points (O1dBCP) are respectively 9.7 and 13.6 dBm. The simulated power consumption increases from 103 to 211 mW when increasing the drain supply from 2 to 3 V. DC testing of the LNA shows a higher power consumption than anticipated (respectively 160 mW and 303 mW) and it was found that this can be attributed to process variations on the threshold of the pHEMT transistors. Adjusting threshold levels in simulations to get corresponding DC behavior shows that an increase in linearity is expected. The newly obtained values are 21.8 dBm (2V) and 26.3 dBm (3V) for the OIP3 and 10.2 dBm (2V) and 13.9 dBm (3V) for the O1dBCP. Two tone OIP3 measurements result in measured levels of 22.2 dBm (2V) and 26.5 dBm (3V) at 28.5 GHz with a 20 MHz tone spacing agreeing very well with the simulated values after threshold compensation.

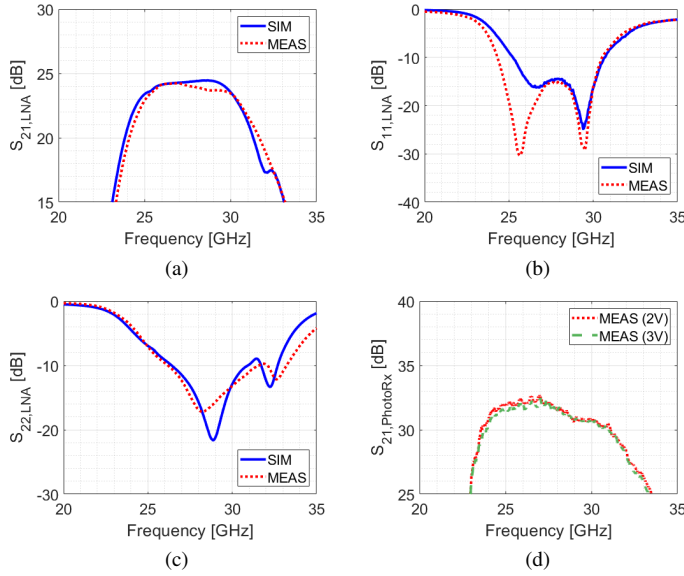


Fig. 8: (a)-(c) LNA S-parameters: Simulations and measurements (d) Normalized opto-electrical response.

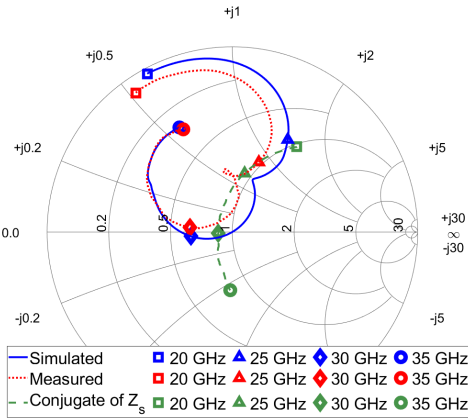


Fig. 9: S_{11} shown on the Smith chart for a 50Ω reference.

C. Noise

In this section the simulated noise performance of the LNA will be discussed (Fig. 10). When the three stages are biased with a 2 V supply, the expected noise figure (NF) ranges between 2.09 dB and 2.16 dB in the frequency range of interest (27.5 to 29.5 GHz). Increasing this supply to 3 V results in increased NF values ranging between 2.26 and 2.32 dB. The input-referred current noise results in a more straightforward interpretation of the sensitivity of the photoreceiver [9]. For the discussed LNA in the targeted frequency band, 2 V and 3 V drain supply results in respectively an input-referred rms current noise below 11.1 and 11.3 $\text{pA}/\sqrt{\text{Hz}}$. When the noise contribution of the series resistance of the photodetector is excluded, this drops to respectively 6.8 and 7.1 $\text{pA}/\sqrt{\text{Hz}}$.

V. STATE OF THE ART

A state of the art comparison is shown in Table I. It can be seen that the input referred current noise lies in between the

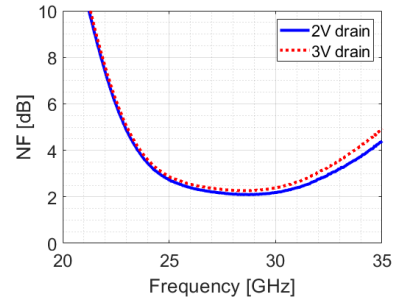


Fig. 10: Simulated noise figure for 2 and 3V drain supply.

values of [13] and [18][19], respectively corresponding to photoreceivers for lower and higher operation frequencies. This is to be expected as the minimum noise figure increases toward higher frequencies [6] and because the passives become lossier at higher frequencies. The transimpedance is comparable to the state of the art apart from the photoreceiver discussed in [18], where multiple amplifier chips are cascaded rather than having a single EIC. Regarding the linearity and power consumption, it can be seen that the presented photoreceiver offers a high linearity while offering low power consumption.

VI. ANALOG RADIO-OVER-FIBER LINK

Two types of data transmission experiments are discussed. Firstly, the performance of the photoreceiver is validated according to 5G New Radio Interface specifications nr257 and nr258 [21]. Secondly, the photoreceiver is tested as part of a high data rate link [22].

A. 5G New Radio Interface Communication

This subsection is an extension on the work presented in [8] where the main addition is a sensitivity analysis. The adopted setup for these measurements is depicted in Fig. 11.

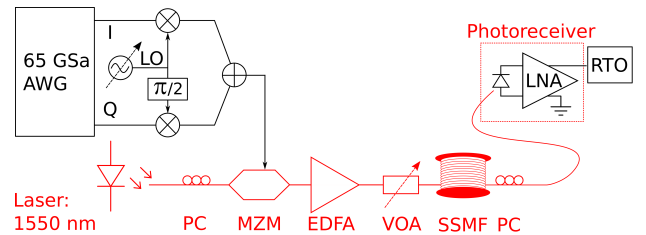


Fig. 11: Setup used for 5G NR Experiments.

The transmitter comprises a continuous wave laser, polarization controller (PC), Mach Zehnder Modulator (MZM), Erbium Doped Fiber Amplifier (EDFA) and Variable Optical Attenuator (VOA). The laser emits 13 dBm, 1550 nm continuous wave light which is subsequently modulated by a quadrature biased MZM. The RF signal fed to the MZM is constructed by an I/Q-mixer (Hittite HMC-1063) where the in-phase (I) and quadrature (Q) signals are generated by an arbitrary waveform generator (AWG, Keysight M8195A) at an IF frequency of 2.5 GHz. The local oscillator (LO) frequency can then be adjusted to choose the carrier frequency of the

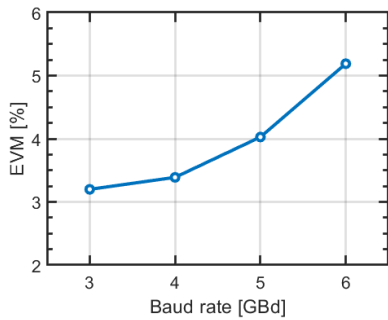


Fig. 14: rms-EVM as a function of the baud rate.

which is well below the 8% 3GPP criterion [23]. Constellation diagrams for 5 and 6 GBd 64-QAM ARoF links are shown in Fig. 15. Using the same setup for sending 4 GBd, 32 QAM over 21 km SSMF results in an rms-EVM of 5.8% (Fig. 16).

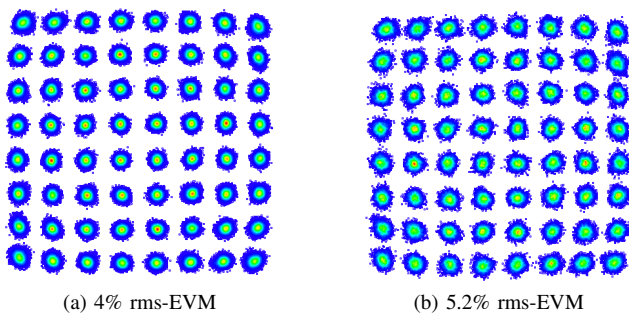


Fig. 15: (a) 5 GBd, (b) 6 GBd at 27.5 GHz – OB2B.

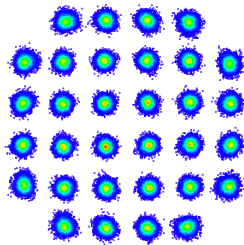


Fig. 16: 4 GBd at 27.5 GHz (5.8% rms-EVM) – 21km SSMF.

VII. CONCLUSION

The design of a narrowband photoreceiver was discussed comprising a Ge photodiode and a dedicated pHEMT GaAs LNA. Some of the key performance values are the external conversion gain of 224 V/W with 3-dB corner frequencies at 23.5 and 31.5 GHz, a minimum noise figure of 2.1 dB and an OIP3 up to 26.5 dBm. The last part of this paper discussed the characterisation of the photoreceiver for two potential applications. First, the device was tested under 5G NR specifications resulting in rms-EVM values below 2.46/3.47% for 100/400-MBaud 16-QAM transmission over the 24.25–29.5 GHz band. Secondly, the photoreceiver was used in a high data rate link showing the potential of sending 36 Gb/s in OB2B configuration at an rms-EVM of 5.2% and 20 Gb/s over 21 km

of SSMF at an rms-EVM of 5.8%. These results showcase the capabilities of narrowband photoreceivers in extreme mobile broadband communication links for next-generation wireless communication.

ACKNOWLEDGMENT

The authors would like to thank VPIphotonics for offering an academic license for their software and the UGent expertise center for nano- and microfabrication NaMiFab for the assembly.

REFERENCES

- [1] J. G. Andrews *et al.*, “What Will 5G Be?,” *IEEE J. Sel. Areas Commun.*, vol. 32, no. 6, pp. 1065–1082, June 2014.
- [2] T. Kawanishi *et al.*, “Wired and Wireless Links to Bridge Networks,” *IEEE Microw. Mag.*, vol. 19, no. 3, pp. 102–111, April 2018.
- [3] A. de la Oliva *et al.*, “An Overview of the CPRI Specification and Its Application to C-RAN-Based LTE Scenarios,” *IEEE Commun. Mag.*, vol. 54, no. 22, pp. 152–159, Feb. 2016.
- [4] M. Pantouvaki *et al.*, “Active Components for 50 Gb/s NRZ-OOK Optical Interconnects in a Silicon Photonics Platform,” *J. Lightw. Technol.*, vol. 35, no. 4, pp. 631–638, Feb. 2017.
- [5] J. Yao, “Microwave Photonics,” *J. Lightw. Technol.*, vol. 27, no. 3, pp. 314–335, Feb. 2009.
- [6] C. Teyssandier *et al.*, “0.1 μ m GaAs pHEMT Technology and Associated Modelling for Millimeter wave Low Noise Amplifiers,” in *European Microwave Integrated Circuits Conference (EuMIC)*, Oct. 2012, pp. 171–174.
- [7] F. Sechi, and M. Bujatti, “Solid-state Microwave High-Power Amplifiers,” 1st ed., Artech House Inc., 2009.
- [8] L. Bogaert *et al.*, “Narrowband Photoreceiver for Analog Radio-over-Fiber in the 24.25 – 29.5 GHz Band,” in *European Conference on Optical Communication (ECOC)*, Sep. 2019, pp. 1–4.
- [9] E. Säckinger, “Broadband Circuits for Optical Fiber Communication,” 1st ed., Wiley-Interscience, 2005.
- [10] H. Kawamura *et al.*, “A 45 - 50 GHz monolithic integrated HFET/MSM OEIC receiver,” in *European Microwave Conference (EUMC)*, vol. 2, Sep. 1995, pp. 990–995.
- [11] E. Säckinger, “The Transimpedance Limit,” *IEEE Trans. Circuits Syst. I, Reg. Papers*, vol. 57, no. 8, pp. 1848–1856, August 2010.
- [12] L. Bogaert *et al.*, “Resonant Optical Receiver Design by Series Inductive Peaking for Sub-6GHz RoF,” *Microw. Opt. Technol. Lett.*, vol. 59, no. 9, pp. 2279–2284, June 2017.
- [13] A. Leven *et al.*, “Design of Narrow-Band Photoreceivers by Means of the Photodiode Intrinsic Conductance,” *IEEE Trans. Microw. Theory Tech.*, vol. 49, no. 10, pp. 1908–1913, Oct. 2001.
- [14] C.S. Walker, “Capacitance, Inductance and Crosstalk Analysis,” 1st ed., Artech House, 1990.
- [15] D.D. Henkes, “A Design Tool for Improving the Input Match of Low Noise Amplifiers,” *High Frequency Electronics*, vol. 6, no. 2, pp. 54–64, Feb. 2007.
- [16] K. Kurokawa, “Power Waves and the Scattering Matrix,” *IEEE Trans. Microw. Theory Tech.*, vol. 13, no. 2, pp. 194–202, March 1965.
- [17] A. Umbach *et al.*, “Technology of InP-Based 1.55- μ m Ultrafast OEM-MICs: 40-Gbit/s Broad-Band and 38/60-GHz Narrow-Band Photoreceivers,” *IEEE J. Quantum Electron.*, vol. 35, no. 7, July 1999.
- [18] A. Miras-Legros *et al.*, “Very high gain, high sensitivity, 40GHz narrowband photoreceiver for clock recovery,” *Electron. Lett.*, vol. 34, no. 3, Feb. 1998.
- [19] S. Fedderwitz *et al.*, “A High Linear and High Power Photoreceiver Suitable for Analog Applications,” in *IEEE Photonics Conference*, Sep. 2012, pp. 308–309.
- [20] T. Umezawa *et al.*, “100-GHz Fiber-Fed Optical-to-Radio Converter for Radio- and Power-Over-Fiber Transmission,” *IEEE J. Sel. Topics Quantum Electron.*, vol. 23, no. 3, May/June 2017.
- [21] 3GPP, “TR 38.815: New Frequency Range for NR (24.25 – 29.5 GHz) – Release 15,” 2018.
- [22] G. Torfs *et al.*, “ATTO: Wireless Networking at Fiber Speed,” *J. Lightw. Technol.*, vol. 36, no. 8, pp. 1468–1477, April 2018.
- [23] 3GPP, “TR 36.104: LTE; Evolved Universal Terrestrial Radio Access (E-UTRA); Base Station (BS) radio transmission and reception - Release 15, v. 15.3.0,” 2018.